Chemical Structure of Conductive Filaments in Tantalum Oxide Memristive Devices and Its Implications for the Formation Mechanism

Thomas Heisig, Kristof Lange, Alexander Gutsche, Kalle Thorben Goß, Sebastian Hambsch, Andrea Locatelli, Tevfik Onur Menteş, Francesca Genuzio, Stephan Menzel, and Regina Dittmann*

Resistive switching in metal oxides is believed to be caused by a temperature and electric field driven redistribution of oxygen vacancies within a nanometer sized conductive filament. Accordingly, gaining detailed information about the chemical composition of conductive filaments is of key importance for a comprehensive understanding of the switching process. In this work, spectromicroscopy is used to probe the electronic structure of conductive filaments in Ta_2O_5-based memristive devices. It is found that resistive switching leads to the formation of a conductive filament with an oxygen vacancy concentration of $\approx 20\%$. Spectroscopic insights provide detailed information about the chemical state of the tantalum cations and show that the filament is not composed of a metallic Ta^0 phase. As an extreme case, devices after an irreversible dielectric breakdown are investigated. These devices feature larger conductive channels with higher oxygen vacancy concentrations. Using the experimental data as input for finite element simulations, the role of thermodiffusion for the formation process of conductive filaments is revealed. It is demonstrated that thermodiffusion is not the dominating effect for the filament formation here but might play a role in accelerating the forming process, as well as in the stabilization of the filament.

1. Introduction

Resistive switching in transition metal oxides has attracted considerable interest for its use in next generation nonvolatile memories[1,2] and emerging technologies, such as neuromorphic[3,4] and in-memory computing.[5] In these devices, the electrical field reversibly modifies the resistance of an oxide layer that is sandwiched between two metal electrodes. It is believed that the resistance change is caused by a voltage driven migration of mobile donor-type point defects, such as oxygen vacancies.[6] Typically, this migration process is localized within a nanometer sized region of the device, the so-called conductive filament.[7,8]

Among the wide variety of resistive switching oxides, TaO_x-based devices are of highest technological interest due to their excellent switching properties in terms of endurance,[9] power consumption,[10] speed[11] and analog switching behavior.[12,13] Accordingly, considerable efforts have been made to clarify the details of the switching mechanism. Despite remarkable progress in recent years, the underlying redox processes that drive resistive switching in TaO_x are still under debate. In particular, the reported composition and size of conductive filaments in TaO_x varies widely in the literature. For example, transmission electron microscopy and electronic transport studies indicate that filaments are highly oxygen deficient with stoichiometries between $TaO_{0.2}$–TaO_1 and are as small as 10 nm,[14,15] whereas other studies report filaments with little oxygen deficiency ($TaO_{2.0}$–$TaO_{2.2}$) and sizes of up to several micrometers.[16,17] Filaments have often been reported to contain oxygen vacancies which are accommodated by a reduction of the valence state of Ta.[16] In contrast to this, transmission

T. Heisig, A. Gutsche, K. T. Goß, S. Hambsch,
S. Menzel, R. Dittmann
Peter Grünberg Institute
Forschungszentrum Jülich GmbH
52425 Jülich, Germany
E-mail: r.dittmann@fz-juelich.de

The ORCID identification number(s) for the author(s) of this article can be found under https://doi.org/10.1002/aelm.202100936.

T. Heisig, A. Gutsche, K. T. Goß, S. Hambsch, S. Menzel, R. Dittmann
JARA-FIT
RWTH Aachen University
52056 Aachen, Germany

K. Lange
Institute of Materials in Electrical Engineering and Information Technology II (IWE 2)
RWTH Aachen University
52056 Aachen, Germany

A. Locatelli, T. O. Menteş, F. Genuzio
Elettra–Sincrotrone Trieste S.C.p.A.
S.S. 14 km–163,5 in AREA Science Park, I-34149 Basovizza, Trieste, Italy

electron microscopy showed an accumulation of Ta within filaments rather than a depletion of oxygen.[14,17,18] Some studies even conclude that the filament contains metallic Ta clusters.[15] Such discrepancies indicate that the filament formation is a complex process that is affected by a manifold of experimental conditions, such as electrical biasing procedure, TaO_x thin film stoichiometry and thickness as well as electrode materials. Furthermore, there is also no consensus on how the filament is formed and modified by the applied voltage. The reason for this is the variety of driving forces that can cause ions to move during resistive switching. The most commonly invoked mechanism relies on a (temperature-accelerated) drift of oxygen ions along the electric potential gradient.[19–21] Recently, an alternative model was proposed in which the ionic motion occurs due to a lateral temperature gradient that is created by Joule heating.[17,22] This process, known as thermodiffusion or thermophoresis, explains the filament formation through a lateral accumulation or depletion of ions. Lastly, the ionic motion due to a concentration gradient, so-called Fick diffusion, has to be considered.[23]

One important cause for the incomplete understanding of the switching mechanism lies in the difficulties of analyzing conductive filaments, which requires methods with high spatial resolution as well as depth sensitivity to detect small chemical changes that occur at the topmost surface layers. Recently, spectromicroscopic methods, such as transmission electron microscopy (TEM) based electron energy loss and energy dispersive X-ray spectroscopy, have been employed to study conductive filaments in TaO_x devices.[14,17,18,24] However, the drawback of these techniques is that they measure the elemental distribution throughout the whole sample thickness, i.e., the TEM lamella. This impedes a direct assessment of the filament composition. Furthermore, many spectromicroscopic techniques that have been used to study TaO_x are not sensitive to the cation oxidation state.[22,25] Accordingly, information on the chemical state of tantalum cations within nanometer sized filaments is missing so far.[16,26] Therefore, it is highly desirable to utilize complementary spectromicroscopic techniques that provide additional information about the composition, size and electronic structure of conductive filaments in TaO_x.

In this work, we use synchrotron-based X-ray photoemission electron microscopy (XPEEM) to detect and quantify switching induced chemical changes in TaO_x memristive devices. We find that the nanometer sized conductive filaments are composed of a suboxide phase with an oxygen vacancy concentration of ≈20%. The spectral signature of the filament reveals that no metallic Ta^0 is present. In addition, spatially resolved Ta 4f XPEEM images were used to evaluate the Ta concentration in the filament and its surroundings. No indication for a lateral accumulation or depletion of Ta was found. Our studies resolve the chemical nature of the conductive filament in a very typical layer stack, namely Ta_2O_5 sandwiched between a Ta electrode and an inert high work function electrode. Based on this knowledge, we are able to draw conclusions about the role of thermodiffusion for the filament formation in this common type of device.

2. Results

To investigate the switching process using photoelectron spectromicroscopy, we fabricated TaO_x memristive devices with graphene electrodes. **Figure 1**a shows a schematic of the device layout. The devices are composed of an oxidizable Ta bottom electrode, a fully oxidized Ta_2O_5 switching layer and an inert single-layer graphene top electrode.

The Ta_2O_5 thin films are amorphous or nanocrystalline since no peaks could be observed by X-ray diffraction analysis (see Figure 8 in the Supporting Information). Moreover, it has been shown in the literature that sputtered Ta_2O_5 thin films exhibit a columnar structure with an oxygen deficiency at the column boundaries.[15] These column boundaries might act as nucleation points for the filament formation as will be discussed later.

Graphene electrodes were selected due to their excellent photoelectron transparency.[27,28] In the asymmetric stack, the low work function Ta electrode forms an ohmic contact to the Ta_2O_5 switching layer, whereas the high work function graphene electrode forms a Schottky interface.[29] The devices were designed to maximize the signal from the Schottky interface, as it is expected to be actively modulated during the switching process.[30,31] Figure 1b displays a secondary electron PEEM image of a single $10 \times 10\ \mu m^2$ device with a structured graphene electrode. To test whether the graphene layer is sufficiently transparent to low energy electrons ($E_{kin} \approx 170$ eV), Ta 4f core level spectra were acquired from an uncovered and a graphene covered region (see Figure 1c). Comparing the intensity of the Ta $4f_{7/2}$ peak shows that the graphene attenuates the signal by a factor of 3.5. While the transmittance of the graphene layer is lower than expected,[28] it is still possible to measure high quality Ta 4f core level spectra with an adequate signal-to-noise ratio. We attribute the lowered transmittance to small amounts of contaminants that might be present at the graphene interface. Possible contaminants are polymer or solvent residues as well as adventitious carbon.[27]

In a next step, it was tested if graphene is a suitable electrode material for resistive switching. For this, devices were electrically characterized by performing quasistatic current-voltage ($I–V$) sweeps. To compare the results to ordinary devices with noble metal electrodes, reference devices with Pt electrodes were prepared and analyzed on the same sample. Figure 1d shows typical $I–V$ curves of a device with graphene electrode (black) and Pt electrode (blue). After an initial electroforming step at high negative voltages (see Figure S1, Supporting Information), both devices show qualitatively similar counter-eightwise resistive switching.[32] If a negative voltage is applied to the top electrode, the device is set from a high resistance state (HRS) to a low resistance state (LRS). Similarly, the devices can be reset from LRS to HRS by applying a positive voltage. In general, graphene devices require higher switching voltages. It is assumed that this difference is caused by the additional series resistance (≈2 kΩ) of the graphene electrode. Based on the qualitative similarities it is argued that the underlying switching mechanism is the same for both device types. A detailed quantitative comparison of the electrode influence on the $I–V$ characteristics can be found in Figure S1 (Supporting Information).

Due to its chemical nature, i.e., being composed of a single layer of carbon atoms, graphene is sensitive to thermal stress and oxidation. Because switching can lead to high temperatures and is typically performed in oxygen containing atmospheres, it is important to study if graphene electrodes are sufficiently stable under prolonged device operation. To test their stability, devices were switched between LRS and HRS for a large number of cycles. Figure 1e shows an endurance measurement of a graphene device switched for 1000 cycles with stable resistive states and an
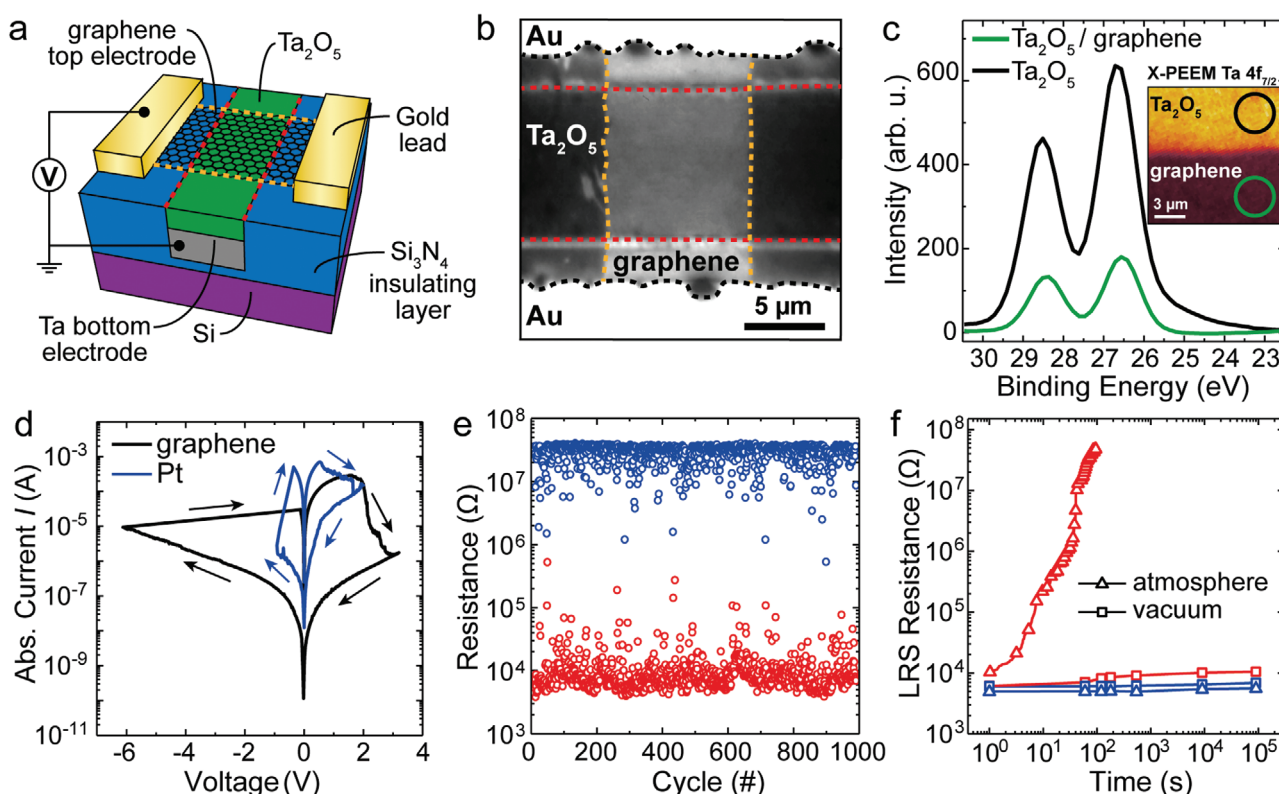
Figure 1. Device layout and resistive switching characteristics. a) Schematic of the device geometry. A Ta_2O_5 layer (green) is sandwiched between a Ta and a graphene top electrode (black honeycomb lattice). The graphene electrode is contacted by gold leads. b) Secondary electron UV-PEEM image of a device. c) Ta 4f XPS spectra extracted from a region without (black) and with graphene electrode (green) acquired at a photon energy of 200 eV. Inset: False color Ta 4f map of the partially graphene covered Ta_2O_5 sample. XPS spectra were extracted from the regions of interest enclosed by the circles. d) Exemplary I–V curves of a device with graphene (black) and Pt (blue) top electrode. e) Endurance measurement of a graphene device with the HRS in blue and the LRS in red. f) Retention behavior of two devices on the same sample with: stable retention (blue) and retention failure (red). Both devices were measured under atmospheric and vacuum conditions.

R^{HRS}/R^{LRS} ratio higher than 10^3. Typical endurance values for graphene devices range between 10^3 to 10^5 cycles. While this is significantly lower compared to the endurance of noble metal devices,[9] it is more than sufficient for the use as a model system to study the switching process. Another important property that the devices must exhibit is a stable retention of at least several hours to ensure that the filament does not change over the time span of an experiment. For approximately half of the devices a stable retention of several days in the LRS was observed, whereas the other half showed a low retention time of just a few seconds to minutes. Figure 1f displays the retention of two prototypical devices, one with and one without stable retention, for different atmospheric conditions. Interestingly, devices that show a retention failure in air have a stable retention in a vacuum environment. This indicates that the retention failure is caused by a reoxidation of the conductive filament through oxygen from the atmosphere. It is surmised that excessive electric stress during the electroforming process can damage the graphene electrode. This allows oxygen to permeate through the graphene. To avoid artifacts from oxidized filaments, only devices with a stable retention were selected for the XPEEM analysis. Based on the spectroscopic and electrical characterization, we concluded that the Ta/Ta_2O_5/graphene model system is ideally suited to study resistive switching in Ta_2O_5 devices using photoelectron spectromicroscopy.

Before the XPEEM analysis of functional devices is presented, it is important to evaluate how oxygen vacancies affect the spectroscopic and electrical properties of TaO_x. It is well known that large amounts of oxygen vacancies in Ta_2O_5 lead to the formation of Ta^{4+}-Ta^0 oxidation states. These reduced states are visible as low binding energy components in the Ta 4f core level spectrum.[25,33,34] For small oxygen vacancy concentrations, however, a rigid shift of the spectrum toward higher binding energies was observed. This was attributed to the n-type doping effect of oxygen vacancies and the resulting shift of the Fermi level toward the conduction band.[35] To complement previous investigations, we prepared and characterized TaO_x thin films over a large range of oxygen stoichiometries (compare **Figure 2**a). All thin films were prepared by reactive sputtering and the oxygen content of the films was adjusted by the reactive gas flow or the deposition rate. After deposition, the thin films were directly transferred into an X-ray photoelectron spectroscopy (XPS) machine under ultrahigh vacuum conditions and analyzed. As expected, there are significant changes in the Ta 4f core level spectrum with changing oxygen content. In the fully oxidized Ta_2O_5 sample, only a single Ta^{5+} peak doublet is visible, whereas oxygen deficient films show additional low binding energy components that can be assigned to Ta^{4+}-Ta^0 oxidation states.[25,33] Fitting of the Ta 4f level allows to deconvolute
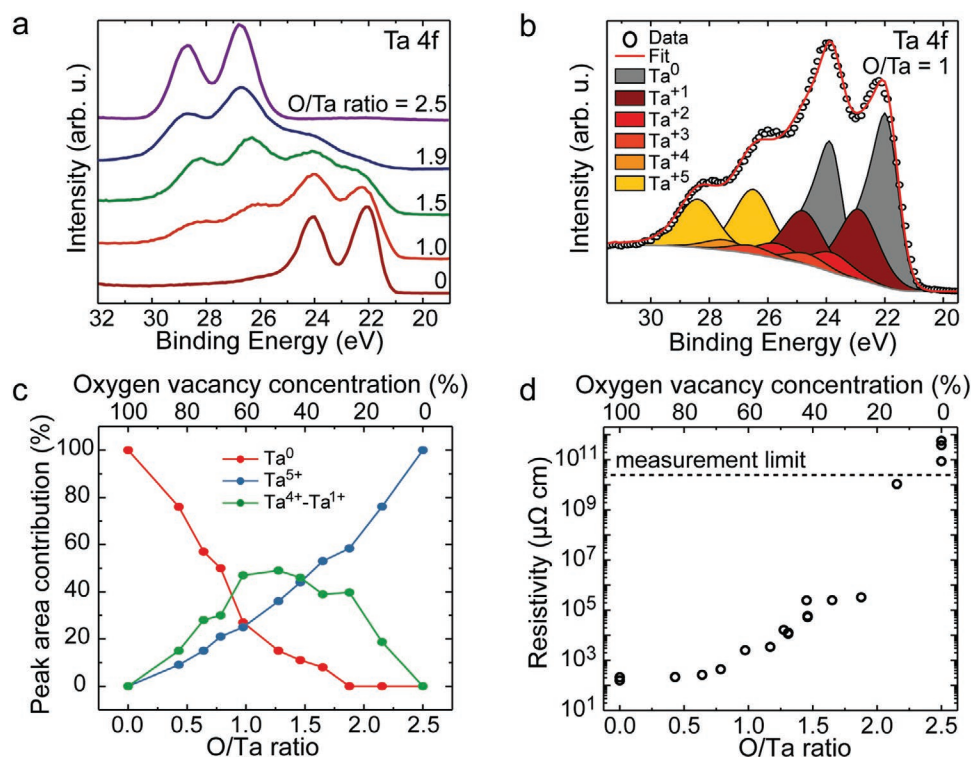
Figure 2. Spectroscopic signature and electrical properties of oxygen vacancies in TaO$_x$. a) Ta 4f core level spectra of TaO$_x$ films with various degrees of oxygen nonstoichiometry. b) Fit of a Ta 4f core level with an O/Ta ratio of 1. c) Peak area contributions of Ta^0, Ta^{5+} and Ta^{4+}-Ta^{1+} components extracted from Ta 4f fits as a function of the oxygen content. d) Resistivity of the TaO$_x$ samples as a function of the oxygen content.

the spectra into individual components and to calculate the O/Ta ratio based on the peak area of each component. A detailed description of the fitting model and the calculation of the oxygen content is given in the Supporting Information. Figure 2b displays an exemplary fit of a TaO$_x$ sample with $x = 1$. The fitting results are summarized in Figure 2c by plotting the peak area fraction of the individual components as a function of the oxygen content. For better visibility, the lower oxidation states Ta^{4+}-Ta^{1+} have been summed up to a single component. The most obvious trend with increasing oxygen content is the linear decrease and increase of Ta^0 and Ta^{5+} respectively. While substantial amounts of Ta^{5+} are present over the whole stoichiometry range, metallic Ta^0 is only detected in samples with an oxygen vacancy concentration above 20%. The combined Ta^{4+}-Ta^{1+} component exhibits a parabolic distribution and shows a maximum at intermediate oxygen contents. Overall, the contribution of the Ta^{4+}-Ta^{1+} components is small compared to Ta^{5+} and Ta^0, which reflects the tendency of TaO$_x$ to form the thermodynamically stable oxidation states.

To explain the resistive switching effect through a change of the oxygen stoichiometry, it is crucial to assess the impact of oxygen vacancies on the electrical resistivity of TaO$_x$. For this, the resistivity of all TaO$_x$ films was measured and plotted against the oxygen content (see Figure 2d). For small oxygen ratios below O/Ta = 0.75, the resistivity is only weakly affected by the oxygen content. This can be explained by the high concentration of Ta^0, which can form a continuous metallic current path through the sample.[15] At intermediate O/Ta ratios from 0.75 to 1.9, the resistivity increases exponentially with the oxygen content. In this region the current transport is dominated by a hopping mecha-

nism.[33,36] With increasing oxygen content, the hopping distance increases and the carrier concentration decreases, resulting in an increased resistivity.[33] Going to even higher oxygen concentrations (O/Ta > 2.1) leads to a pronounced jump in resistivity. This indicates a transition from hopping conduction to a highly insulating oxide. The fully oxidized Ta$_2$O$_5$ samples exceeded the maximum resistivity that could be measured by the setup. Nevertheless, the results demonstrate that introducing 20% oxygen vacancies into a fully oxidized Ta$_2$O$_5$ film reduces the resistivity by at least five orders of magnitude.

Based on these insights, the investigation is extended to functioning Ta$_2$O$_5$ devices with graphene electrodes. For this purpose, a device was switched several times in air and kept in the LRS. One should mention here that the purpose of this work is to study the filament in the early stage after forming and not the degradation after repeated switching. Therefore, the PEEM investigations have only been performed on devices switched for a few times and not over the whole cycle time shown in Figure 1e. Afterward, the sample was transferred into the PEEM analysis chamber. In a first attempt to locate the filament, the device was analyzed by acquiring a photoelectron threshold XPEEM image stack. **Figure 3**a displays a secondary electron image of the device taken at a start voltage bias of 3.5 V. The image shows that the graphene electrode features a large crack in the middle of the device, leaving parts of the device area uncovered (dashed orange line). This type of graphene defect was commonly observed in our devices and is likely caused by mechanical stress during the transfer and structuring process. Nevertheless, the electrical characterization confirmed that the device was fully operational and we do
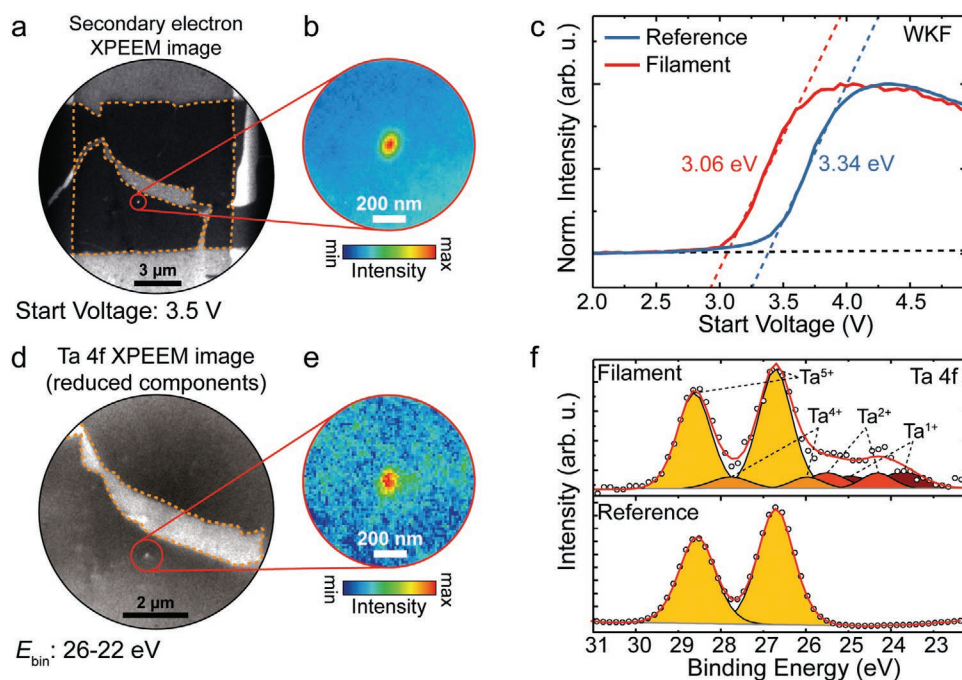
Figure 3. Spectromicroscopy of a device in the LRS. a) Secondary electron XPEEM image of a device in the LRS acquired at an electron kinetic energy of 3.5 eV. The dashed orange line shows the active device area covered by graphene. b) Magnified false color map of the area enclosed by the red circle in (a). c) Photoelectron threshold spectra extracted from the filament and the surrounding area. d) Ta 4f core level XPEEM image of reduced Ta^{x+} components acquired by averaging images taken at binding energies from 26 to 22 eV. e) Magnified false color map of the area enclosed by the red circle in (d). f) Ta 4f core level spectra of the filament (top) and the surrounding area (bottom). The filament spectrum was extracted from a central 3×3 pixel region (red pixel in panel e).

not expect the defect to have an impact on the switching process. Upon close examination of the active device area, a small region of interest with increased photoelectron intensity was identified (compare Figure 3b). Extracting the photoelectron threshold spectrum from this region reveals a work function shift toward lower energies by 0.3 eV (Figure 3c). This shift is indicative for *n*-type doping, which is expected for an oxygen vacancy rich filament.[16,37] To obtain chemical information from the region of interest an image stack spanning the photoelectron energies across the Ta 4f core-level was acquired. Figure 3d shows the core level photoelectron XPEEM image of the previously identified filament candidate. The image was generated by averaging individual images acquired at binding energies from 22 to 26 eV. This energy range corresponds to the reduced tantalum oxidation states (compare Figure 2b). Therefore, a high photoelectron intensity signifies an increased concentration of Ta states with lower valence. It is noted that the high intensity from the graphene-free area is caused by the overall much higher Ta signal and no reduced states were detected in this area. Figure 3e shows a magnified false color map of the feature. Its position coincides with the position of the feature observed in the secondary electron image. The Ta 4f spectrum of the feature is displayed in Figure 3f and exhibits a characteristic low binding energy shoulder that can be assigned to Ta^{4+}–Ta^{1+} oxidation states.[25] In contrast, the reference spectrum is composed entirely of Ta^{5+}. Based on these spectroscopic results we identify this small region as the conductive filament. Assuming charge neutrality within the filament, the O/Ta ratio can be calculated from the peak area fraction of the individual components. Fitting of the filament spectrum yields an O/Ta value of 2.0 ± 0.1, which equals an oxygen vacancy concentration of 20 ± 4%. Similar oxygen vacancy concentrations were observed previously in micrometer sized TaO_x filaments.[16] Importantly, no indications for a metallic Ta^0 component could be identified. This is in good agreement with the results derived from the reference films in Figure 2c, which also show no metallic contribution for this stoichiometry. Due to the high surface sensitivity of XPEEM, the measured oxygen vacancy concentration can be considered as an average value of the top 2–3 nm of the Ta_2O_5 switching layer. This, however, represents a significant portion of the 8 nm thick switching layer. Furthermore, it is expected that the strongest changes occur at the Schottky interface.[19]

Besides containing spectroscopic information, our XPEEM data further provides valuable insights about the lateral distribution of Ta and O within and around the filament, which is crucial to study the thermophoresis effect. **Figure 4**a shows two Ta 4f core level XPEEM images. The first image was generated by averaging over all individual images taken at binding energies from 22 to 31 eV. Accordingly, the image represents the complete Ta 4f core level and the photoelectron intensity is proportional to the total Ta concentration. The second image was processed in an analogous manner to the image shown in Figure 3d, that is, by averaging images taken at low binding energies (E_{bin} = 26–22 eV). Thus, the intensity in the image is proportional to the concentration of Ta^{x+} in lower oxidation states. Figure 4b displays the normalized radial intensity of both images starting from the filament core propagating into the surrounding region. A radial intensity profile was chosen because thermodiffusion is expected to occur isotropically in
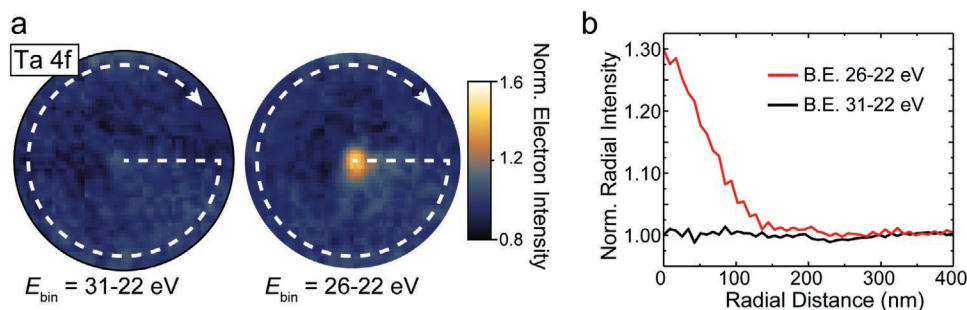
Figure 4. Local Ta concentration in the vicinity of the conductive filament. a) False color Ta 4f XPEEM images of the filament and adjacent regions. The images were generated by summing individual images over the full core level $E_{bin} = 31–22$ eV (left) and over the energies representative for reduced components $E_{bin} = 26–22$ eV (right). b) Rotationally averaged intensity profiles integrated along the white dashed lines in (a). The intensity profiles are normalized to the background signal far away from the filament.

all directions starting from a central hot-spot, i.e., the filament. The intensity profile of the image corresponding to the total Ta concentration shows only small deviations from the average intensity within the signal-to-noise ratio, indicating a homogenous Ta distribution inside and around the filament. In contrast, the second image representing the reduced states, exhibits a maximum intensity in the filament core, which gradually declines until the background intensity is reached. Considering that the concentration of reduced Ta states is proportional to the oxygen vacancy concentration, the intensity profile can be understood as a measure of the filament size. Using the full width at half maximum (FWHM) as an estimate of the filament size, a diameter of 120 nm could be assumed. However, one should keep in mind that the XPEEM microscope resolution in the chosen experimental configuration was in the 60 nm range estimated from the X-ray absorption spectroscopy images. By simulating the intensity profiles for a given filament size and instrument broadening (see Supplementary Information), we estimate a filament size (diameter) of about 70 nm at the topmost surface layers and could clearly state that the filament diameter is within an interval of 50 nm-90 nm. Atomic force microscopy analysis shows topographic changes within a diameter of 116 nm (see Figure S4, Supporting Information), however, these changes cannot be identified one-to-one with the region of increased oxygen vacancy content since the region of Joule heating will likely exceed the filament diameter. These topological changes might hint at a crystallization of the filament region, but we could clearly prove in our earlier studies that the filament remains amorphous despite the observed change of the topography. [16] This could be confirmed by more recent transmission electron microscopy studies on devices more similar to this study.

The study was extended to the characterization of devices that were subject to an irreversible or "hard" dielectric breakdown. While conductive filaments in such devices are evidently not representative for operational devices, they nevertheless can provide valuable information about device failure mechanisms that arise from excessive electrical stress. **Figure 5**a shows a device after a capacitive discharge that occurred in situ inside the XPEEM analysis chamber. It is assumed that the discharge was induced by an electric arc due to the high voltage bias between the sample and the objective (extractor) lens. The discharge produced a clearly visible defective region at the edge

of the crossbar structure. Although the device was visibly damaged it remained electrically connected to the bottom electrode, exhibiting very little resistance. This verifies that a conducting path through the oxide was formed. However, no attempt to reset the device into a HRS was successful. Hard dielectric breakdowns are commonly observed in memristive devices if the electroforming or set process is performed without an active current or voltage limiter.[2,38] Therefore, a hard breakdown can be considered as an extreme case of the switching process, which leads to the creation of a permanent conductive path.[37] Figure 5b shows a false color map of the defective region that displays the lower binding energy components. In comparison to the conductive filament in Figure 3, the reduced region is much larger ($\approx 2 \times 0.5$ μm²) and the Ta 4f spectrum shows a stronger reduction. Fitting of the core level yields an O/Ta ratio of 1.7 ± 0.1. This corresponds to an oxygen vacancy concentration of $32 \pm 4\%$. Interestingly, the contribution of the individual components differs significantly from TaO_x reference films with a similar stoichiometry.

Most importantly, no metallic Ta component is present in the defective region whereas comparable sputtered films have a Ta^0 fraction of 8%. The missing Ta^0 is compensated by an increased fraction of Ta^{1+} giving rise to a complex spectral shape of the core level. Accordingly, the electronic structure of suboxide phases with the same oxygen stoichiometry can differ depending on the fabrication or reduction process. This is not surprising if one considers that the electric field induced breakdown takes place on very short timescales below one nanosecond and under extreme conditions, i.e., high electric fields and temperatures.[11,39]

To investigate the role of thermodiffusion for the formation of conductive filaments, finite element simulations have been performed based on the filament size and the electrical forming data of our devices. We used the most likely filament diameter of 70 nm as starting point and investigated how the results of the simulation are influenced by the filament size (see Supporting Information). For the simulation, three equations are solved describing the current and heat flow and the transport of oxygen vacancies (a detailed description of the model can be found in the Supporting Information). Using the model, the experimental electroforming I–V curve of the device investigated by XPEEM (see Figures 3 and 4) was reproduced by fitting the filament conductivity to the experimental data. As we
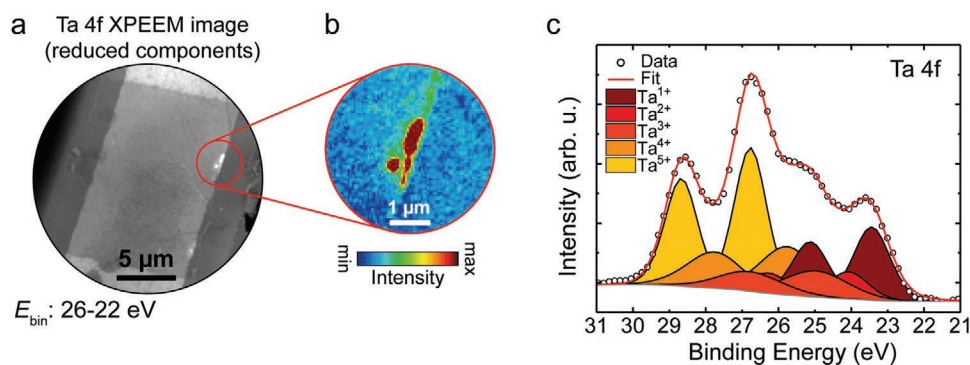
Figure 5. Spectromicroscopy of a device after a capacitive discharge. a) Ta 4f core level XPEEM image of reduced Ta^{x+} components acquired by averaging images taken at binding energies from 26 to 22 eV. b) Magnified false color map of the damaged area enclosed by the red circle in (a). c) Ta 4f core level spectra extracted from the red pixels in (b).

are only interested in the forming process, only the sweep from 0 to −5 V is considered in the simulation rather than the full sweep. In the model it is assumed that a conductive path is pre-existing in the oxide. This is necessary for the formation of a local hot-spot and the generation of a temperature gradient. Such a pre-existing conductive path might be created by other mechanism such as a highly nonlinear field-driven oxide conductivity or oxygen vacancy rich regions formed the column boundaries of the Ta$_2$O$_5$ thin films.[15] The results are presented in **Figure 6**a. At a voltage of −4.34 V, the current rapidly increases over multiple orders of magnitude, marking the forming event. With the current flowing mainly through a filament region with a radius of 35 nm, the forming event is immediately followed by an increase of the maximum device temperature by several hundred Kelvin. Based on the experimentally determined conductivity values for TaO$_x$ with ≈20% oxygen vacancies (see Figure 2d), we initially assume an increased conductivity by six orders of magnitude within the filament, and then keep the conductivity outside of the filament constant. The resulting current and temperature gradient along a radial cut line in the oxide at half oxide height is shown in Figure 6b. Due to the thermal conductivity of the Ta$_2$O$_5$ layer, a temperature gradient develops over a comparably large distance, with the highest temperatures emerging in the central part of the filament. As a temperature gradient is the driving force for thermodiffusion, it is conceivable that ions accumulate and/or deplete within this region. Therefore, we studied the ion migration due to thermodiffusion for selected activation enthalpies of migration and voltages in the electroforming process. Figure 6c shows the radial oxygen vacancy distribution for an activation enthalpy of ΔH = 1.6 eV (blue) and 0.8 eV (red). This selection is motivated by the experimentally determined value for oxygen tracer diffusion (1.6 eV) and the lower boundary for a conceivable migration barrier (0.8 eV).[40] Using an activation enthalpy of ΔH = 1.6 eV, we find that the maximum oxygen vacancy concentration reaches an equivalent dopant concentration of ≈0.3%. However, the increase in concentration mainly occurs after the forming event. The influence of thermodiffusion is even lower for smaller applied voltages. The situation changes, however, if a small migration barrier of ΔH = 0.8 eV is considered. In this case, a vacancy transport toward the filament can be observed, leading to an accumula-

tion of vacancies in the filament and to a depletion of vacancies around the filament. Figure 6d shows a 2D view of the temperature and oxygen vacancy distribution for the highest applied voltage and the lowest migration barrier. This case represents the strongest influence of thermodiffusion that we expect to occur in our devices. Although significant thermodiffusion can be observed, the maximum vacancy concentration remains below an equivalent dopant concentration of 2%. Here it is noted that we also simulated an activation enthalpy of ΔH = 3.6 eV to study the diffusion of tantalum ions. Due to the very high activation energy, however, no thermodiffusion occurred under these conditions.

3. Discussion and Conclusions

Based on our experimental observations and simulation results, we can draw important conclusions about the chemical structure of conductive filaments in Ta$_2$O$_5$ memristive devices and their formation mechanism. The XPEEM analysis provides experimental evidence that conductive filaments in Ta/Ta$_2$O$_5$/graphene devices are composed of an oxygen deficient suboxide phase with an oxygen vacancy concentration of ≈20%. Based on the similar $I–V$ characteristics of graphene and Pt devices we surmise that the same switching mechanism is operating in both device types. With respect to the oxygen vacancy concentrations and the presence of substoichiometric phases, these results are also in line with our earlier studies.[16] These studies have been based on samples with detached electrodes which needed a special softly bonded top electrode and an unusual forming polarity, resulted resulting in a very uncommon shape and size of the filament. With this work, we could improve the generality of our PEEM studies by using samples with a working top electrode and a common forming procedure. Accordingly, we expect that our results are transferable to similar Ta$_2$O$_5$ memristive device architectures that exhibit a Schottky interface.

Using TaO$_x$ reference films with various oxygen nonstoichiometries, we established a correlation between the oxygen vacancy concentration and the electrical conductivity. We find that small changes in the oxygen stoichiometry have a large impact on the resistivity, especially for low oxygen vacancy
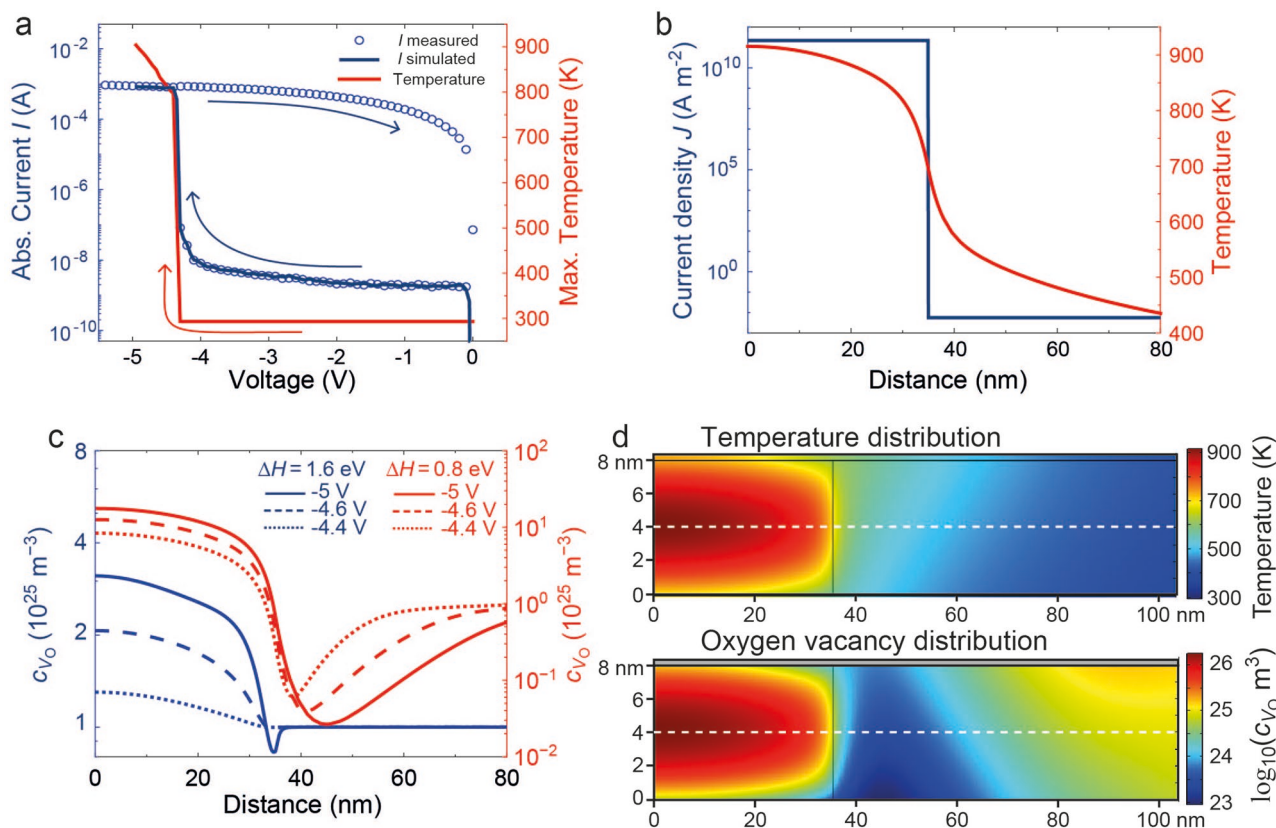
**ADVANCED
SCIENCE NEWS**
www.advancedsciencenews.com

**ADVANCED
ELECTRONIC
MATERIALS**
www.advelectronicmat.de

Figure 6. Device simulation of ionic motion along temperature gradients for a filament radius of 35 nm. a) Simulated and measured I–V curves and simulated maximum device temperature during electroforming. The measured voltage sweep back to 0 V is not part of the simulation. b) Current density and temperature distributions along a radial cut line at half oxide height for an applied voltage of −5 V. c) Oxygen vacancy concentrations along the same cut line as in (b) for selected activation enthalpies and voltages. A vacancy concentration of $c_{V_o} = 10^{25}$ m^{-3} corresponds to a dopant concentration of ≈0.1%. d) 2D view of the temperature and oxygen vacancy distribution within the oxide layer at $V = -5$ V and $\Delta H = 0.8$ eV. The white dashed line indicates the position of the cut lines in (b) and (c).

concentrations. Accordingly, the resistance change between LRS and HRS can be explained by small modifications of the local oxygen vacancy concentration, which induce a strong change in the bulk resistance of the Ta$_2$O$_5$ layer. Besides their effect on the bulk resistance, oxygen vacancies also modulate the Schottky barrier, which further increases the impact of changing oxygen vacancy concentrations on the device resistance.[28] Considering that the I–V characteristics of our devices show an asymmetric nonlinear I–V behavior in the HRS and an ohmic behavior in the LRS (compare Figure S1, Supporting Information), it can be assumed that the modulation of the Schottky barrier plays an important role in the switching process. Therefore, the filament region near the graphene electrode probed by PEEM is the most relevant part of the filament and changes in the oxygen content deeper below the surface play a minor role for the conductivity and the switching process.

Considering that the conductive filament contains only 20% oxygen vacancies, it appears unlikely that a metallic phase is responsible for the electronic transport in the LRS, which was theorized as a possible switching mechanism.[15] This is confirmed by a deconvolution of the Ta 4f core level spectrum of the filament into its individual components. The spectrum shows no signs of a metallic Ta^0 component. Here it is noted that even with insufficient spatial microscope resolution, a metallic phase

would still be visible in the core level spectrum due to the pronounced chemical shift of Ta^0. Consequently, we can exclude a phase separation into the thermodynamically stable phases, Ta and Ta$_2$O$_5$, as a possible switching mechanism.[41] Our experimental insights highlight that resistive switching in TaO$_x$ is not governed by the thermodynamic characteristics of the Ta–O system, but rather involves the creation and of a kinetically stable suboxide phase.

The important question remains how oxygen deficient filaments are formed. To explain the filament formation, typically two models are invoked: A temperature accelerated drift of oxygen anions along the electric field gradient or thermodiffusion of ions along a temperature gradient. To distinguish between both mechanisms, the local atomic composition of the filament and its surrounding can be studied. While the drift of oxygen vacancies along the electric field results mainly in a vertical redistribution of oxygen anions, thermodiffusion causes lateral diffusion of ions. In Ta$_2$O$_5$, both ionic species, oxygen and tantalum, have been found to redistribute due to thermodiffusion.[14,22] Using the information from the Ta 4f XPEEM images, we investigated if lateral ion diffusion also occurs in our devices. Our results show that the filament and its surrounding have a homogenous Ta distribution within the measurement accuracy. This result is not surprising if one

considers that cation diffusion in Ta_2O_5 is orders of magnitude slower compared to oxygen diffusion.[40] It should be noted that cation diffusion increases for a decreasing oxygen content in TaO_x.[42] Thus, cations could become mobile within the filamentary region after it has been formed. In our case, however, the switching layer is stoichiometric and thus the cation diffusion is hindered. Since oxygen is more mobile, it is conceivable that a filament is formed due to thermodiffusion of oxygen anions away from a filament. This process would result in a depletion and accumulation of oxygen within and around the filament, respectively.[22] While our experimental results confirm the oxygen depletion within the filament, it is not possible to determine if additional oxygen has accumulated in regions around the filament. This is because the Ta 4f core level is not sensitive to excess oxygen.[43]

To resolve the question how an oxygen vacancy rich filament forms, we simulated if thermodiffusion can explain the experimental data. The results clearly show that the impact of thermodiffusion is too small to explain the significant accumulation of oxygen vacancies that was observed by XPEEM. Even for the most optimistic set of simulation parameters, −5 V and a migration barrier of $\Delta H = 0.8$ eV for stoichiometric Ta_2O_5, a vacancy concentration of below 2% was obtained within the filament. The filament radius of 35 nm used in the simulation marks a lower bound for radii observed in experiment. Additional simulations were performed with a radius of 55 nm, which is near the upper end of the estimated filment size range. In that case, the equivalent dopant concentration remains below 0.8% for $\Delta H = 0.8$ eV and below 0.11% for $\Delta H = 1.6$ eV, which corresponds to a relative increase of less than 3%. For smaller radii, a higher concentration could be achieved but then unrealistically high temperatures are required as shown in Figure S7 (Supporting Information). In addition, the conductivity of the filamentary region would assume values that are a lot higher than the experimental values shown in Figure 2d for the determined oxygen vacancy content of 20%. For the chosen filament size, the assumed conductivity of the filament is consistent with the experimentally determined one. Moreover, the model assumes that a filament has already been created by some other mechanism such as a highly nonlinear field-driven oxide conductivity or oxygen vacancy rich regions formed the column boundaries of the Ta_2O_5 thin films.[15] An initial homogenous conductance did not lead to any Joule heating. While the forming process cannot be explained by purely thermal effects, thermodiffusion might nevertheless play a role in accelerating the forming process, as well as in the stabilization of the filament. In the thermodiffusion simulations, ionic drift was deliberately neglected to study a pure thermodiffusion (and diffusion) mechanism. However, previous simulations combining both drift and thermodiffusion showed that ionic drift is a much stronger effect.[21,44,45] Thus, as major process for the electroforming effect, an oxygen exchange reaction followed by oxygen migration appears to be more realistic.[44]

It is important to note that the cation diffusion barrier decreases significantly for substoichiometric TaO_x.[42] This might explain why device stacks starting with strongly substoichiometric films behave differently and Ta redistribution as well as thermodiffusion plays a more pronounced role.[14,17,18]

However, in device stacks starting with a stoichiometric Ta_2O_5 layer a very similar scenario with respect to the chemical structure of the filament and its formation mechanism can be expected.

4. Experimental Section

Device Fabrication: A Ta bottom-electrode and Ta_2O_5 switching layer stack was fabricated by structuring and etching 40 nm deep trenches into a Si/Si_3N_4 substrate using optical lithography and CF_4 reactive ion beam etching. The trenches were filled by depositing a 33 nm Ta bottom electrode followed by an 8 nm Ta_2O_5 switching layer using RF-magnetron sputtering. After the lift-off, single layer graphene (*Graphenea*, Spain) was deposited onto the sample as described in detail in ref. [46]. The graphene electrodes were structured into $30 \times 10\ \mu m^2$ rectangles by optical lithography and oxygen plasma etching. The graphene was contacted by metal leads consisting of 10 nm Pt and 60 nm Au, which were deposited by electron beam evaporation and structured through optical lithography and a lift-off process.

Reactive Sputtering of TaO_x Thin Films: TaO_x thin films were prepared using reactive RF-magnetron sputtering. The oxygen content was controlled through the reactive gas flow, the deposition rate, and the pumping speed. A detailed description of deposition parameters can be found in the Supporting Information.

X-Ray Photoelectron Spectroscopy of TaO_x Thin Films: TaO_x samples were directly transferred under UHV conditions ($p < 2 \times 10^{-8}$ mbar) into a NanoESCA microscope equipped with a Channeltron and operated in the spectroscopy mode. For all samples, a survey scan and a Ta 4f core level spectrum was acquired. No carbon contamination could be detected and no change of the stoichiometry over the time span of 72 h was observed. The data were quantified using *CasaXPS* version 2.3.16. Details of the core level fitting can be found in the Supporting Information.

Electrical Characterization: I–V sweeps were performed with a Keithley 2611A SourceMeter and all voltages were applied to the top electrode. A current compliance of 1 mA was used for the electroforming process, 50 μA for the SET, and no compliance was used for the RESET. Endurance measurements were acquired by using voltage pulses with a pulse length of 2 ms, a set voltage of −4 V and a reset voltage of 3.2 V. A current compliance of 30 μA was used for the set and no compliance was used for the reset pulse. The sheet resistance of the TaO_x reference films was measured in a standard Van-der-Pauw configuration by contacting four corners of a square $1 \times 1\ cm^2$ sample via ultrasonic Al wire bonding using a Hall Effect Measurement System Model 8404. The resistivity was obtained by multiplying the sheet resistance with the thin film thickness, which was measured using X-ray reflectivity.

Photoemission Electron Spectromicroscopy: The XPEEM experiments were performed using the SPELEEM microscope operating at the Nanospectroscopy beamline at Elettra synchrotron laboratory, Trieste, Italy. Images were acquired at a photon energy of 200 eV. Image stacks were taken at increasing kinetic energies with a step size of 0.05 and 0.15 eV for photoelectron threshold and core level electron imaging, respectively. Photoemission spectra from the filament in Figure 3 were extracted from 3×3 pixel sized region of interest and the reference spectra were extracted from regions close to the filament. The spatial resolution of the PEEM was determined to be ≈60 nm. Quantification of the Ta 4f core level was performed with the same procedure that was used for the TaO_x reference films. The uncertainty of the O/Ta ratio was estimated based on the robustness of the core level fit.

Supporting Information

Supporting Information is available from the Wiley Online Library or from the author.

**ADVANCED
SCIENCE NEWS**

www.advancedsciencenews.com

**ADVANCED
ELECTRONIC
MATERIALS**

www.advelectronicmat.de

Conflict of Interest

The authors declare no conflict of interest.

Data Availability Statement

The data that support the findings of this study are available from the corresponding author upon reasonable request.

[1] R. Waser, R. Dittmann, C. Staikov, K. Szot, *Adv. Mater.* **2009**, *21*, 2632.

[2] H. S. P. Wong, H. Y. Lee, S. Yu, Y. S. Chen, Y. Wu, P. S. Chen, B. Lee, F. T. Chen, M. J. Tsai, *Proc. IEEE* **2012**, *100*, 1951.

[3] Z. Wang, M. Yin, T. Zhang, Y. Cai, Y. Wang, Y. Yang, R. Huang, *Nanoscale* **2016**, *8*, 14015.

[4] M. Prezioso, F. Merrikh-Bayat, B. D. Hoskins, G. C. Adam, K. K. Likharev, D. B. Strukov, *Nature* **2015**, *521*, 61.

[5] D. Ielmini, H.-S. P. Wong, *Nat. Electron.* **2018**, *1*, 333.

[6] R. Waser, M. Aono, *Nanosci. Technol.* **2007**, *6*, 158.

[7] J. P. Strachan, M. D. Pickett, J. J. Yang, S. Aloni, A. L. David Kilcoyne, G. Medeiros-Ribeiro, R. S. Williams, *Adv. Mater.* **2010**, *22*, 3573.

[8] D. H. Kwon, K. M. Kim, J. H. Jang, J. M. Jeon, M. H. Lee, G. H. Kim, X. S. Li, G. S. Park, B. Lee, S. Han, M. Kim, C. S. Hwang, *Nat. Nanotechnol.* **2010**, *5*, 148.

[9] M. J. Lee, C. B. Lee, D. Lee, S. R. Lee, M. Chang, J. H. Hur, Y. B. Kim, C. J. Kim, D. H. Seo, S. Seo, U. I. Chung, I. K. Yoo, K. Kim, *Nat. Mater.* **2011**, *10*, 625.

[10] K. X. Shi, H. Y. Xu, Z. Q. Wang, X. N. Zhao, W. Z. Liu, J. G. Ma, Y. C. Liu, *Appl. Phys. Lett.* **2017**, *111*, 223505.

[11] A. C. Torrezan, J. P. Strachan, G. Medeiros-Ribeiro, R. S. Williams, *Nanotechnology* **2011**, *22*, 485203.

[12] U. Böttger, M. von Witzleben, V. Havel, K. Fleck, V. Rana, R. Waser, S. Menzel, *Sci. Rep.* **2020**, *10*, 16391.

[13] W. Song, W. Wang, H. K. Lee, M. Li, V. Y.-Q. Zhuo, Z. Chen, K. J. Chui, J.-C. Liu, I.-T. Wang, Y. Zhu, *Appl. Phys. Lett.* **2019**, *115*, 133501.

[14] Y. Ma, J. M. Goodwill, D. Li, D. A. Cullen, J. D. Poplawsky, K. L. More, J. A. Bain, M. Skowronski, *Adv. Electron. Mater.* **2019**, *5*, 1800954.

[15] C. M. M. Rosario, B. Thöner, A. Schönhals, S. Menzel, A. Meledin, N. P. Barradas, E. Alves, J. Mayer, M. Wuttig, R. Waser, N. A. Sobolev, D. J. Wouters, *Nanoscale* **2019**, *11*, 16978.

[16] K. Skaja, C. Bäumer, O. Peters, S. Menzel, M. Moors, H. Du, M. Bornhöfft, C. Schmitz, V. Feyer, C. L. Jia, C. M. Schneider, J. Mayer, R. Waser, R. Dittmann, *Adv. Funct. Mater.* **2015**, *25*, 7154.

[17] Y. Ma, D. Li, A. A. Herzing, D. A. Cullen, B. T. Sneed, K. L. More, N. T. Nuhfer, J. A. Bain, M. Skowronski, *ACS Appl. Mater. Interfaces* **2018**, *10*, 23187.

[18] Y. Ma, P. P. Yeoh, L. Shen, J. M. Goodwill, J. A. Bain, M. Skowronski, *J. Appl. Phys.* **2020**, *128*, 194501.

[19] S. Menzel, M. Waters, A. Marchewka, U. Böttger, R. Dittmann, R. Waser, *Adv. Funct. Mater.* **2011**, *21*, 4487.

[20] J. H. Hur, M.-J. Lee, C. B. Lee, Y.-B. Kim, C.-J. Kim, *Phys. Rev. B* **2010**, *82*, 155321.

[21] A. Marchewka, B. Roesgen, K. Skaja, H. Du, C. Jia, J. Mayer, V. Rana, R. Waser, S. Menzel, *Adv. Electron. Mater.* **2016**, *2*, 1500233.

[22] S. Kumar, C. E. Graves, J. P. Strachan, E. M. Grafals, A. L. D. Kilcoyne, T. Tyliszczak, J. N. Weker, Y. Nishi, R. S. Williams, *Adv. Mater.* **2016**, *28*, 2772.

[23] P. R. Mickel, A. J. Lohn, B. Joon Choi, J. Joshua Yang, M. X. Zhang, M. J. Marinella, C. D. James, R. Stanley Williams, *Appl. Phys. Lett.* **2013**, *102*, 223502.

[24] G. S. Park, Y. B. Kim, S. Y. Park, X. S. Li, S. Heo, M. J. Lee, M. Chang, J. H. Kwon, M. Kim, U. I. Chung, R. Dittmann, R. Waser, K. Kim, *Nat. Commun.* **2013**, *4*, 2382.

[25] S. Kasatikov, E. Filatova, S. Sakhonenkov, A. Konashuk, A. Makarova, *J. Phys. Chem. C* **2019**, *123*, 6849.

[26] A. Kindsmüller, C. Schmitz, C. Wiemann, K. Skaja, D. J. Wouters, R. Waser, C. M. Schneider, R. Dittmann, *APL Mater.* **2018**, *6*, 046106.

[27] J. Kraus, R. Reichelt, S. Günther, L. Gregoratti, M. Amati, M. Kiskinova, A. Yulaev, I. Vlassiouk, A. Kolmakov, *Nanoscale* **2014**, *6*, 14394.

[28] C. Baeumer, C. Schmitz, A. Marchewka, D. N. Mueller, R. Valenta, J. Hackl, N. Raab, S. P. Rogers, M. I. Khan, S. Nemsak, M. Shim, S. Menzel, C. M. Schneider, R. Waser, R. Dittmann, *Nat. Commun.* **2016**, *7*, 12398.

[29] K. Cheng, N. Han, Y. Su, J. Zhang, J. Zhao, *Sci. Rep.* **2017**, *7*, 41771.

[30] R. Waser, *J. Nanosci. Nanotechnol.* **2012**, *12*, 7628.

[31] J. J. Yang, M. D. Pickett, X. Li, D. A. A. Ohlberg, D. R. Stewart, R. S. Williams, *Nat. Nanotechnol.* **2008**, *3*, 429.

[32] R. Muenstermann, T. Menke, R. Dittmann, R. Waser, *Adv. Mater.* **2010**, *22*, 4819.

[33] I. Goldfarb, F. Miao, J. J. Yang, W. Yi, J. P. Strachan, M. X. Zhang, M. D. Pickett, G. Medeiros-Ribeiro, R. S. Williams, *Appl. Phys. A: Mater. Sci. Process.* **2012**, *107*, 1.

[34] M. H. Lee, C. S. Hwang, *Nanoscale* **2011**, *3*, 490.

[35] K. Skaja, M. Andrä, V. Rana, R. Waser, R. Dittmann, C. Baeumer, *Sci. Rep.* **2018**, *8*, 10861.

[36] C. E. Graves, N. Dávila, E. J. Merced-Grafals, S. T. Lam, J. P. Strachan, R. S. Williams, *Appl. Phys. Lett.* **2017**, *110*, 123501.

[37] B. Xiao, S. Watanabe, *Nanoscale* **2014**, *6*, 10169.

[38] Q. Li, J. Xing, Z. Sun, F. Jing, H. Xu, in *Proc. – IEEE Int. Symp. Circuits Syst*, IEEE, Baltimore, USA, May **2017**.

[39] M. von Witzleben, T. Hennen, A. Kindsmüller, S. Menzel, R. Waser, U. Böttger, *J. Appl. Phys.* **2020**, *127*, 204501.

[40] U. N. Gries, H. Schraknepper, K. Skaja, F. Gunkel, S. Hoffmann-Eifert, R. Waser, R. A. De Souza, *Phys. Chem. Chem. Phys.* **2018**, *20*, 989.

[41] F. Miao, J. P. Strachan, J. J. Yang, M. X. Zhang, I. Goldfarb, A. C. Torrezan, P. Eschbach, R. D. Kelley, G. Medeiros-Ribeiro, R. S. Williams, *Adv. Mater.* **2011**, *23*, 5633.

[42] B. Xiao, X. Yu, S. Watanabe, *ACS Appl. Electron. Mater.* **2019**, *1*, 585.

[43] T. Tsuchiya, H. Imai, S. Miyoshi, P. A. Glans, J. Guo, S. Yamaguchi, *Phys. Chem. Chem. Phys.* **2011**, *13*, 17013.

[44] A. Marchewka, R. Waser, S. Menzel, in *2017 Int. Conf. Simul. Semicond. Process. Devices*, IEEE, Kamakura, Japan, September **2017**, p. 133.

[45] S. H. Lee, J. Moon, Y. J. Jeong, J. Lee, X. Li, H. Wu, W. D. Lu, *ACS Appl. Electron. Mater.* **2020**, *2*, 701.

[46] X. Liang, B. A. Sperling, I. Calizo, G. Cheng, C. A. Hacker, Q. Zhang, Y. Obeng, K. Yan, H. Peng, Q. Li, *ACS Nano* **2011**, *5*, 9144.